In-situ generation and global property profiling of metal nanoclusters by ultraviolet laser dissociation-mass spectrometry

Zheyi Liu[1,2†], Zhaoxian Qin[3,7†], Chaonan Cui[4], Zhixun Luo[4,7], Bing Yang[5], You Jiang[6], Can Lai[2,7], Zhipeng Wang[1,2], Xiaolei Wang[1,2], Xiang Fang[6], Gao Li[3*], Fangjun Wang[2,7*], Chunlei Xiao[1*] & Xueming Yang[1]

[1]*State Key Laboratory of Molecular Reaction Dynamics, Dalian Institute of Chemical Physics, Chinese Academy of Sciences, Dalian 116023, China;*
[2]*CAS Key Laboratory of Separation Sciences for Analytical Chemistry, Dalian Institute of Chemical Physics, Chinese Academy of Sciences, Dalian 116023, China;*
[3]*State Key Laboratory of Catalysis, Dalian Institute of Chemical Physics, Chinese Academy of Sciences, Dalian 116023, China;*
[4]*State Key Laboratory for Structural Chemistry of Unstable and Stable Species, Institute of Chemistry, Chinese Academy of Sciences, Beijing 100190, China;*
[5]*Dalian National Laboratory for Clean Energy, Dalian Institute of Chemical Physics, Chinese Academy of Sciences, Dalian 116023, China;*
[6]*National Institute of Metrology, Beijing 100013, China;*
[7]*University of Chinese Academy of Sciences, Beijing 100049, China*

Metal nanoclusters are promising nanomaterials with unique properties, but only a few ones with specific numbers of metal atoms can be obtained and studied up to now. In this study, we establish a new paradigm of *in-situ* generation and global study of metal nanoclusters with different sizes, constitutions, and charge states, including both accurate constitution characterization and global activity profiling. The complex mixtures of metal nanoclusters are produced by employing single-pulsed 193-nm laser dissociation of monolayer-protected cluster (MPC) precursors within a high-resolution mass spectrometry (HRMS). More than 400 types of bare gold nanoclusters including novel multiply charged (2+ and 3+), S-/P-doped, and silver alloy ones can be efficiently generated and accurately characterized. A distinct size (1 to 142 atoms)- and charge (1+ to 3+)-hierarchy reactivity is clearly observed for the first time. This global cluster study might greatly promote the developments and applications of novel metal nanoclusters.

metal nanocluster, ultraviolet laser dissociation, mass spectrometry, global property profiling, size- and charge-hierarchy

1 Introduction

Metal nanoclusters are widely recognized as the bridge phases between metal atoms and their bulk counterparts and exhibit unique properties such as discrete electronic structure and molecule-like property [1]. The atomically precise monolayer-protected cluster (MPC) nanomaterials composed of internal metal cores and peripheral ligands are well developed in recent years, providing profits to structural diversity and potential applications in a few interdisciplinary fields such as photochemistry, catalysis, chemo-sensing, drug delivery, and bio-imaging [2–7]. However, only the

---

†These authors contributed equally to this work.
*Correspondence authors (email: chunleixiao@dicp.ac.cn; wangfj@dicp.ac.cn; gaoli@dicp.ac.cn)

metal nanoclusters with specific numbers of atoms such as Au_{25}, Au_{38}, Au_{102}, and Au_{144} could be synthesized due to the cluster stability up to now [1]. The chemical properties of metal clusters are dependent on their sizes, constitutions, and unique geometric and electronic structures, which cannot be deduced by linear extension of the properties of known nanoclusters [8]. It is still challenging to produce a variety of metal nanoclusters with diverse constitutions and sizes, as well as globally profile their properties.

Mass spectrometry (MS) has been widely coupled with sophisticated metal-cluster sources to investigate the properties of metal clusters [9,10], which are usually generated through the sputtering of the metal target by energetic particle beams or laser beams. The metal vapor of free atom could be generated and then fused into different sizes of metal clusters in a designed aggregation zone, exemplified by the widely used laser vaporization cluster sources [11–13] and magnetron cluster sources [14,15]. The constitution and size distribution of metal nanoclusters could be tuned by controlling the vapor concentration, temperature, and pressure. Moreover, the cluster ion beam produced by laser desorption of passivated nanocrystals has been also reported [16], and the sulfur-doped gold clusters with single positive charge ($[Au_nS_m]^+$) were generated [17]. Recently, a pioneering study of ultraviolet photodissociation (UVPD) of the monolayer-protected Au_{25} and Au_{36} clusters was reported, which directly generated small and mono-charged bare gold nanoclusters [18]. *In-situ* generation and global profiling platform for metal nanoclusters are still under development, which greatly limits the discovery and application of novel nanoclusters with specific properties.

In this work, we employed the Au_{25} and Au_{144} MPC precursors with precise constitutions and sizes for generating metal nanoclusters *via* ultraviolet laser-induced photodissociation. We introduced a 193-nm ultraviolet laser into the dissociation chamber of an HRMS system, where the MPC precursors were effectively activated and dissociated by the laser shot, leading to the generation of metal nanoclusters with diverse constitutions, including bare metal clusters, alloy metal clusters, and nonmetallic-atom-doped clusters. Some novel metal clusters that were difficult to be generated by conventional metal-cluster sources, such as the gold clusters with 2+ and 3+ charge states, were successfully obtained in this laser dissociation platform, in addition to the mono-charged ones. Further, the effects of size (1 to 142 Au atoms), S or P atom doping, silver alloys, and charge states (1+ to 3+) on the stabilities and activities of Au nanoclusters are systematically investigated by *in-situ* HRMS profiling.

2 Experimental

2.1 Materials

The wet chemistry of metal nanoclusters is receiving upris-

ing research interest and the synthetic procedures of monolayer-protected metal clusters (MPCs) have been well developed [19]. Here, the MPC precursors including $Au_{25}(Cy)_{18}$, $Au_{25}(PPh_3)_{10}(SPh)_5Cl_2$, $Au_{25}(PPh_3)_{10}(PET)_5Cl_2$, $Au_{144}(PET)_{60}$, and $Au_{144}(SC_6H_{13})_{60}$ were synthesized according to our previous methods (Cy, cysteine; PPh_3, triphenylphosphine; SPh, benzenethiol; PET, 2-phenylethanethiolate;) [20–22].

2.2 Ultraviolent laser-HRMS system for the MPC precursor dissociation

All the mass spectrometry experiments were performed on a Thermo Exactive plus EMR HRMS system. A 193-nm ArF excimer laser (GAM LASER, Inc., EX50 EXCIMER LASER) was introduced into the higher-energy collision dissociation (HCD) chamber (Figure S1A). The charge detector in the back of the HCD chamber was removed and an MgF_2 window was implemented in the conflat flange of the HCD chamber. The excimer laser was operated in the pulsed mode with the pulse-length of 5 ns and the frequency of 3 Hz (with about 300 ms interval between adjacent shots) and adjusted to insure an intensity of 1–2 mJ/pulse at the MgF_2 window. The MPC precursors were dissolved into the electrospray ionization (ESI) buffer (70% dichloromethane/30% methanol, *v/v*) with a concentration of 1 mg mL^{-1}; the corresponding MPC ions were normally produced and introduced into the HRMS system by the nano-ESI with a spray voltage of 1.5 kV in the positive mode. The sample injection flow rate was 300 nL min^{-1}.

For the MPC precursor characterizations, the mass resolution of HRMS was set at 140,000 ($m/z = 200$) for Au_{25} and 17,500 for Au_{144} MPC precursors. Then, the MPC precursor ions were guided into the laser-dissociation chamber (the HCD normalized collision energy (NCE) was set at 0 during the whole process). A single-shot laser irradiation with a pulse length of 5 ns was applied for the dissociation of MPC precursors and the generation of the complex metal nanoclusters. The complex fragment clusters were cooled down within the dissociation chamber (20 mTorr N_2) for about 100 ms and then transferred to the orbitrap analyzer for the high-throughput characterizations before the next laser-shot (with about 300 ms interval between adjacent shots) arrived. All spectra of the fragment metal nanoclusters were collected with a mass resolution of 140,000 ($m/z = 200$). The HCD dissociation of the MPC precursors was also performed with NCE of 20–160 for the comparison.

To investigate the chemisorption activity of gas reactants over the complex metal nanoclusters, carbon monoxide (CO) or acetylene (C_2H_2) gas were introduced into the HCD chamber. After laser dissociation, the fragment metal clusters were trapped in the HCD chamber and reacted with the gas reactants (1 *v*% reactant gas mixed with 99 *v*% N_2, about 20 mTorr in total, 298 K) for about 100 ms. The chemisorption

intermediate and product ions were then transferred to the orbitrap analyzer in about 10 ms and characterized with a mass resolution of 140,000 ($m/z = 200$) before the next laser shot arrived. All the HRMS spectra were collected in the profile mode (continuous mode). The spectra were manually interpreted, and the theoretical spectra were calculated by enviPat (https://www.envipat.eawag.ch) [23]. All the data were publicly available in the figshare (doi: 10.6084/m9.figshare.12520391).

3   Results and discussion

3.1   *In-situ* generation and stability evaluation of the metal nanoclusters

Figure 1a presents the dissociated fragment nanoclusters of two positive-charged Au_{25} MPC precursors (Figure S2). Upon a single-shot laser irradiation (5 ns), almost all of the peripheral ligands (*i.e.*, $–SC_8H_9/–SPh$, $–PPh_3$, and $–Cl$) of MPC precursors were stripped away. Meanwhile the Au_{25} kernel was completely dissociated to produce bare Au_n^+ nanoclusters with consecutive size (n: 1–22, Figure 1a). By contrast, conventional high-energy collision-induced dissociation (HCD) only partially detached the peripheral ligands of MPC precursors without inducing efficient fragmentation of the Au_{25} kernel (Figure S3). The fragmentation efficiency of our system was much higher than that in the work of Black *et al.* [18], in which 10 shots of a 193-nm laser with similar pulse energy were applied to fragment $Au_{25}(SR)_{18}$ MPC precursors. The $Au_{25}(SR)_{18}$ and $[Au_{25}(SR)_5(PPh_3)_{10}Cl_2]^{2+}$ were different types of Au_{25} topological clusters with different metal core structures and charge states [22]. The ionization of neutral $Au_{25}(SR)_{18}$ in ESI was assisted by the addition of Na^+ or NH_4^+, which was easily dissociated upon photon activation, while the 2+-charged core of $[Au_{25}(SR)_5(PPh_3)_{10}Cl_2]^{2+}$ more preferred to be dissociated due to the charge-repulsion effect after stripping out-layer ligands.

Moreover, the generation and the distribution of fragment Au_n^+ nanoclusters in the laser dissociation were mainly dominated by the intrinsic metal kernel of MPC precursors (Figure 1a). The Au_{25} MPC precursors with different peripheral ligands exhibited similar fragmentation patterns upon single-shot laser dissociation (Figure 1a), indicating the relative intensities of fragment Au_n^+ nanoclusters were controlled by their thermodynamic stability. We speculate that the 193-nm ultraviolet photons mainly excite the peripheral ligands and the energy deposition of intense laser pulse might strip away the peripheral ligands efficiently followed with the overall metal kernel fragmentation. Of note, a series of $[Au_nS_x]^+$ and $[Au_nP_y]^+$ clusters are also generated *via* the cleavage at the S–C and P–C bonds during the laser-induced photodissociation (Figure 1b). Multiple sulfur atoms can

remain in the relative large $[Au_nS_x]^+$ clusters ($n>15$); for example, all the 5 sulfur atoms survive in the case of $[Au_{23}S_5]^+$ (Figure 1c). However, the PPh_3 ligands are detached from the clusters' surface much easier than the thiolate ligands and only one phosphorus atom could be retained in the fragment nanoclusters at most, which is consistent with our previous observations [24,25]. The intensities of Au_n^+ nanoclusters with odd-numbers are usually higher than those with even-numbers, attributed to the shell-closing effect where all valence electrons are paired in the electron shell [26]. Similar even-odd intensity variation is also observed in the $[Au_nS]^+$ and $[Au_nP]^+$ nanoclusters (Figure 1d). The ratio of $[Au_nS]^+/Au_n^+$ increases along with the increasing numbers of gold atoms in general (Figure 1e); the intensity of $[Au_nS]^+$ ($n≥20$) is higher than that of the corresponding Au_n^+. It is worth noting that the intensity of $[Au_nS]^+$ ($n≤7$) is extremely low relative to $[Au_n]^+$, and the $[Au_nS]^+$ ($n≥8$) nanoclusters are much more stable (Figure 1e). For the $[Au_nP]^+$, the relative ratio of $[Au_nP]^+/Au_n^+$ shows a zigzag-like shape, indicating that the preferential bonding of the phosphorus atom with $[Au_nP]^+$ species of the even-number (Figure 1e). Obviously, the general stability and the mass abundances of certain Au nanoclusters are strongly related to their constitutions, geometric/electronic structures, and whether or not an addition of sulfur and phosphorus atoms can efficiently tune the surface charge distribution and site-related properties hence to activate or passivate the metal nanoclusters [27].

Then, more comprehensive Au nanoclusters were generated by laser dissociation of Au_{144} MPC precursors (Figures S4). Similarly, the complete explosion of the Au_{144} kernel is observed and the produced nanoclusters is dominated by nanoclusters ranging from Au_{14}^{2+} to Au_{142}^{2+} (Figure 1f and S5). The odd-even peak intensity variation of Au_n^{2+} clusters is opposite to the case of Au_n^+ due to the shell-closing effect (Figure S6). Of note, the Au_{60}^{2+} cluster which bears a magic number of 58 valance electrons shows the most mass abundance among all the observed species (Figure 1f). A series of $[Au_nS]^{2+}$ clusters are also produced (Figure 1g) and the intensity of Au_nS^{2+} ($n≥120$) species is comparable to that of the corresponding Au_n^{2+} (Figure 1h). Compared with the mono-charged Au_n^+, both even- and odd-numbered Au_nS^{2+} were produced, but without significant even-odd alternation of the intensities. Therefore, both the sulfur doping and charge state can significantly alter the electronic structure and stability of the gold clusters *via* charge redistribution and orbital hybridization, which is crucial for cluster property modulation as demonstrated in previous theoretical-calculation studies [28]. In addition, 3+-charged nanoclusters ranged from Au_{50}^{3+} to Au_{128}^{3+} are also observed with lower intensity (Figures 1i and 1j), indicating that metal clusters with multiple charges including 2+ and 3+ can be feasibly generated in laser dissociation of MPC precursors. This is hardly achieved by conventional metal-cluster sources *via* the particle beam or
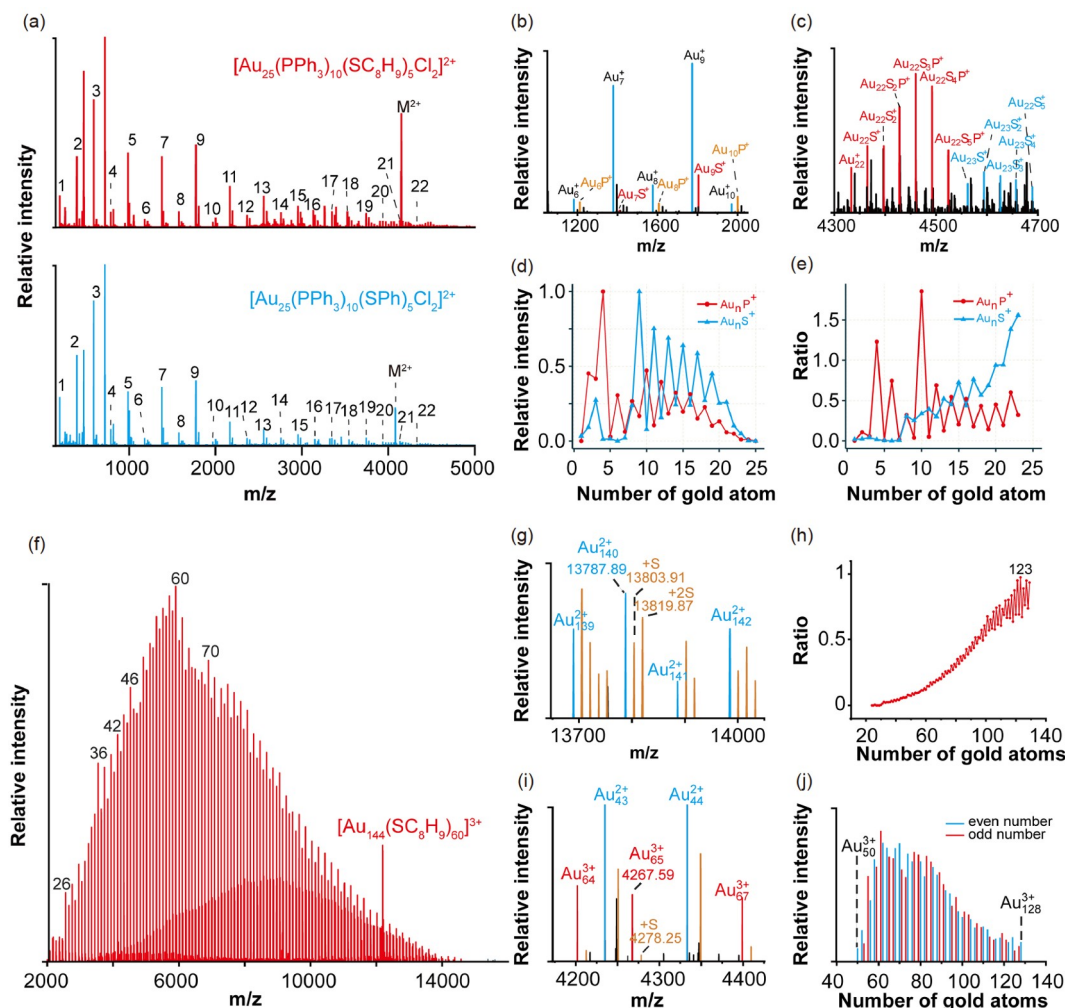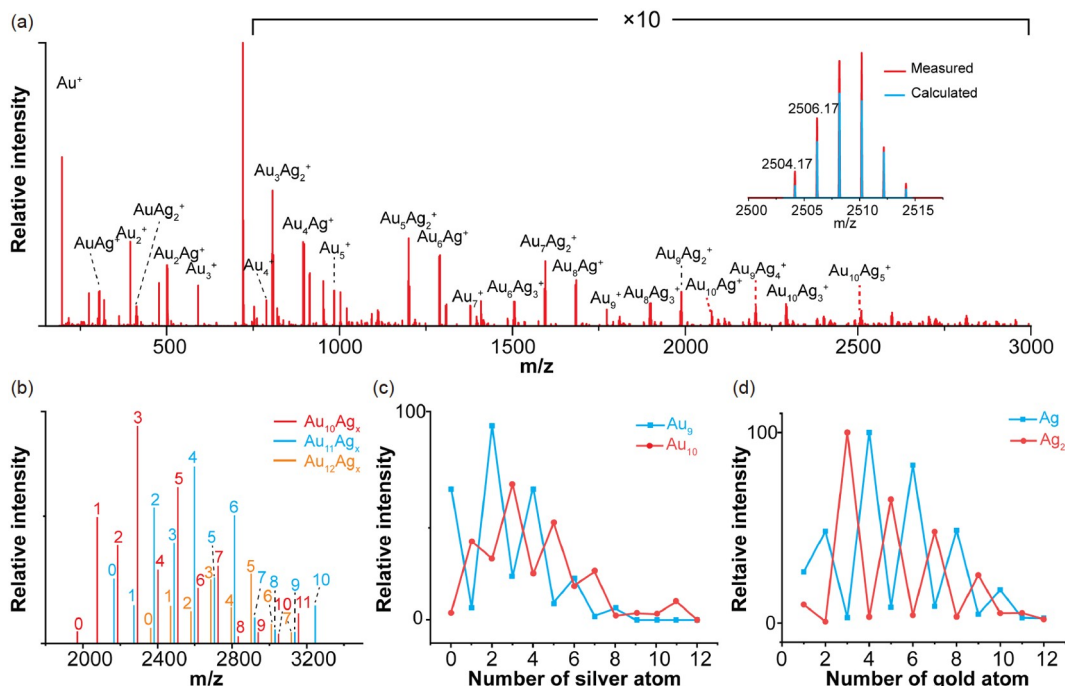
Figure 1 The generation and stability evaluation of gold nanoclusters by single-shot (5 ns) laser dissociation of the MPC precursors. (a) Au_n^+ nanoclusters generated by laser dissociation of $[Au_{25}(PPh_3)_{10}(SC_8H_9)_5Cl_2]^{2+}$ (upper) and $[Au_{25}(PPh_3)_{10}(SPh)_5Cl_2]^{2+}$ (lower), where *n* indicates the size of nanoclusters; (b and c) enlarged views of Au_n^+ and $[Au_nS_xP_y]^+$ nanoclusters dissociated from $[Au_{25}(PPh_3)_{10}(SC_8H_9)_5Cl_2]^{2+}$; (d) the relative intensities of $[Au_nS_x]^+$ and $[Au_nP_y]^+$ species with different sizes; (e) the ratios of $[Au_nS]^+/Au_n^+$ and $[Au_nP]^+/Au_n^+$; (f) the generation of gold nanoclusters with multiple-charged states by laser dissociation of $Au_{144}(SC_8H_9)_{60}$, where *n* indicates the size of nanoclusters; (g) the 2+-charged gold nanoclusters with S atoms; the *m/z* space between Au_n^{2+} and Au_nS^{2+} clearly confirms the charge states of the nanoclusters; (h) the relative ratios of $[Au_nS]^{2+}/Au_n^{2+}$ with different sizes; (i) the generation of Au_n^{3+} nanoclusters; the charge states can be determined by the appearance of adduct satellites with *m/z* +10.66 (sulfur atom, charge: 31.97/10.66=3); (j) the distribution of Au_n^{3+} nanoclusters (*n*: 50–128, the overlapping peaks with Au_n^{2+} are excluded). Detection conditions: *T*=298 K, *P*=20 mTorr (pure N_2), pulsed 193 nm laser with 1–2 mJ and a diameter of ~2 mm, 3 Hz (pulse length 5 ns, with about 300 ms interval). No collision energy was applied during the whole process (color online).

laser ablation of metal targets followed with metal vapor condensation [9,10,29]. This unique property of multiple-charged metal nanoclusters provides important insights for developing effective catalysts.

Further, the alloy nanoclusters consisting of two or more different metal species could efficiently tune the cluster activity [30]. The Au–Ag alloy nanoclusters were further generated by laser dissociation of the $[Ag_{12}Au_{13}(PPh_3)_{10}Cl_8]^+$ precursor (Figure 2 and Figure S7). The silver atoms are typically less than gold atoms in the alloy nanoclusters, indicating that the silver species might be easier to be detached during the laser dissociation (Figure 2a). The maximum size of the generated alloy clusters is the $Au_{10}Ag_{11}$ and $Au_{11}Ag_{10}$, while Au_{12} could retain up to 7 Ag atoms (Figure 2b). Si-

milarly, strong size-dependent intensity variation is observed in the $Au_xAg_y^+$ nanoclusters (Figure 2c and 2d).

Overall, the gold and alloy nanoclusters with extremely diverse physical and chemical properties in size, constitution and charge state are feasibly generated by laser dissociation of MPC precursors within HRMS. Further, *in-situ* and global HRMS characterization of the complex metal clusters has been achieved. The aforementioned results demonstrate that the constitution and property of gold nanoclusters can be efficiently tuned by precise synthesis and controllable laser dissociation of the MPC precursors (with specific sizes and compositions). Considering that multiple-charged (+2 and +3) and S-/P-doped metal clusters can be efficiently generated by this novel strategy, the scope of gas-phase metal

Figure 2 The generation and stability evaluation of Au–Ag alloy nanoclusters by single-shot (5 ns) laser dissociation of the MPC precursors. (a) the generation of $Au_xAg_y^+$ nanoclusters upon laser dissociation of Au–Ag alloy MPC precursors, (*x*: the number of gold atoms; *y*: the number of silver atoms); inset: the measured and calculated distributions of isotopic patterns of $Au_{10}Ag_5^+$; (b) the extracted intensities of alloy nanoclusters with 10, 11 and 12 gold atoms; (c) the intensity alteration of alloy nanoclusters with 9 and 10 gold atoms; (d) the intensity alteration of alloy nanoclusters with 1 and 2 silver atoms. Detection conditions were the same as that in Figure 1 (color online).

cluster investigations and potential applications could be greatly expanded.

3.2 Global activity profiling of the metal nanoclusters.

Having demonstrated the size- and charge-hierarchy in determining the metal cluster abundance and stability [31], we then globally probed the cluster chemical property *via* CO adsorption [32–34]. The gas reagent of 1% CO mixed with 99% N_2 (20 mTorr) was introduced into the HCD chamber of the HRMS to incubate with the produced Au nanoclusters for about 100 ms, and then transferred into the orbitrap analyzer for the *in-situ* characterization before the next laser shot (3 Hz, pulse length 5 ns, with about 300 ms interval) arrived. Figure 3a presents *in-situ* CO adsorption over Au nanoclusters for global activity profiling, where the adsorption products reveal the altered activity of corresponding nanoclusters with different geometric and electronic structures [35,36]. Specifically, the Au_n^+ (*n*: 1–20) clusters can adsorb at least one CO and a maximum adsorption of eight CO was observed on the Au_9^+, Au_{11}^+ and Au_{15}^+ (Figure S8). The product distribution and CO maximum adsorption capacity of Au_nP^+ and Au_nS^+ are similar to the corresponding Au_n^+ clusters of *n*=4–6 (Figure 3b and Figure S8). However, different adsorption behaviors are observed with *n*≥7. Although the maximum CO adsorption number is 8 for both Au_9^+ and Au_9S^+, the patterns of product intensity distribution differ from each other (Figure S8b). Besides, Au_{11}^+ has a maximum CO adsorption number of 8, while $Au_{11}S$ can only adsorb up to 5 CO molecules (Figure 3c). The same phenomena were also observed for Au_nP^+, which had a smaller CO adsorption number than Au_n^+ with *n*≥8 (Figure S8). Therefore, the addition of sulfur atoms and phosphor atoms can significantly alter the activity of Au clusters, attributed to their modulation on the geometric and electronic structure of Au clusters.

In the case of the multiple-charged nanoclusters generated *via* laser dissociation of the Au_{144} MPC precursor (Figure 3d), a charge-induced enhancement of CO adsorption capacity is clearly observed. For example, the Au_{16}^+–Au_{20}^+ clusters only can adsorb less than 5 CO molecules (Figure S9a), while the Au_{16}^{2+}–Au_{20}^{2+} clusters could adsorb up to 10 CO molecules (Figure S9b). It is worth mentioning that the charge-induced enhancement of CO-donating characteristics was also found in the previous literatures, but generally limited to 1− and 1+ states [37,38]. There is still lack of a highly-efficient method to generate multiple-charged metal clusters as the ionization of the second electron from the mono-positively-charged clusters is much more difficult than that of the first electron [37,38]. The relative distribution patterns of CO adsorption products of the Au_n^{2+} clusters (*n*: 15–140) are summarized and systematically compared. A strong size-dependent effect is observed for the CO adsorption behavior (Figure 3f). The maximum absorption of 12 CO molecules is observed for Au_{26}^{2+} and Au_{27}^{2+} (Figure
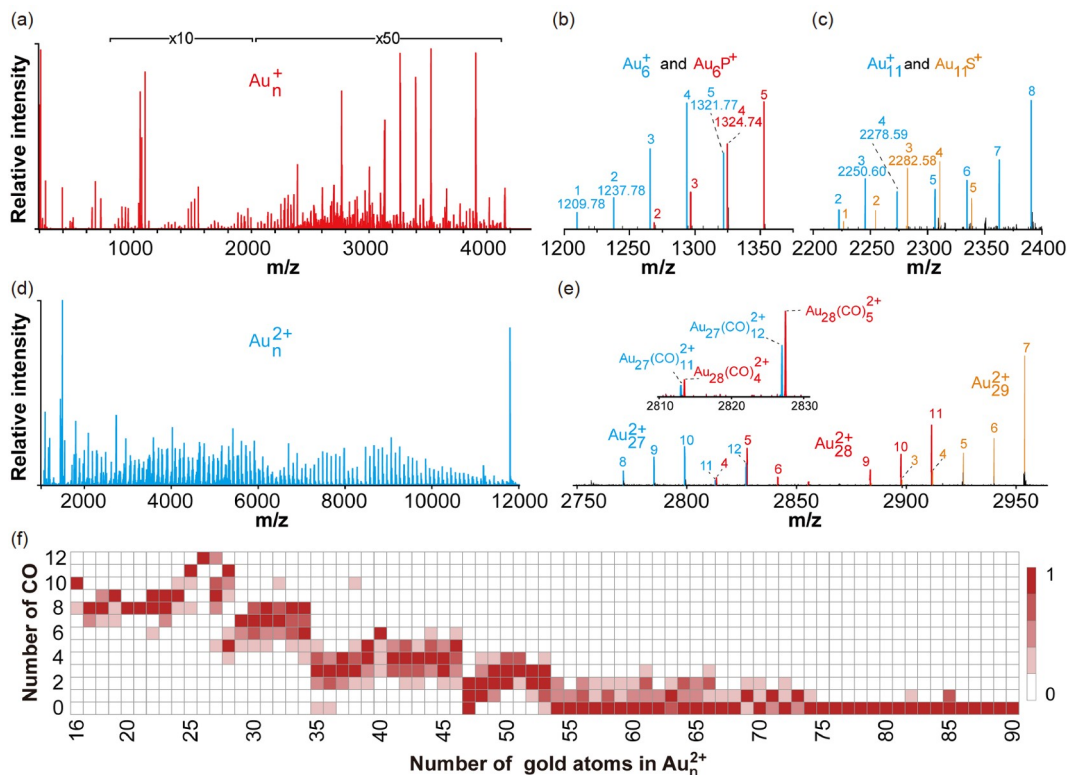
Figure 3 Global activity profiling of Au nanoclusters by incubating with CO gas reactant (20 mTorr, 1 *v*% CO and 99 *v*% N$_2$), followed by *in-situ* and global MS characterization. (a) A typical MS spectrum of Au$_n^+$ clusters with CO; (b) the enlarged spectrum of Au$_6^+$ and Au$_6$S$^+$ interacting with CO; (c) the enlarged spectrum of Au$_{11}^+$ and Au$_{11}$S$^+$ interacting with CO; (d) the typical MS spectrum of Au$_n^{2+}$ clusters with CO; (e) the enlarged spectrum of Au$_{27}^{2+}$ (blue), Au$_{28}^{2+}$ (purple) and Au$_{29}^{2+}$ (orange) interacting with CO; (f) the overall distribution of CO adsorption on the Au$_n^{2+}$ clusters (*n*: 16–90). The detection conditions are the same as that in Figure 1 (color online).

3e). The CO adsorption activity is step-wisely decreased from Au$_{15}^{2+}$ to Au$_{140}^{2+}$, and several crucial transition points could be clearly observed at the gold atom numbers of 28/29, 34/35, 46/47 and 53/54 (Figures 3e and 3f). For example, up to 11 CO could be adsorbed on Au$_{28}^{2+}$, while this number dramatically decreases to 7 for Au$_{29}^{2+}$ (Figure 3e). The dramatic activity changes of Au$_n^{2+}$ nanoclusters at these pivotal points indicate the significant alternations on their geometric and electronic structures. The CO adsorption activity of Au$_n^{2+}$ nanoclusters is greatly reduced at *n*≥54, and no CO adsorption is observed at *n*≥86 (Figure 3f).

We have further profiled the activity of AuAg alloy clusters, and the replacement of Au with Ag in the cluster ions greatly compromises the activity of Au clusters (Figure 4). For example, Au$_7^+$ clusters can adsorb up to 6 CO, while the Au$_4$Ag$_3^+$ clusters only can adsorb up to 3 CO molecules (Figure 4a and c). Similar phenomena can be observed for the Au$_x$Ag$_y^+$ clusters with *x*+*y*=9, 11 and 13, respectively (Figure 4d–f). The increasing silver content in the Au$_x$Ag$_y^+$ clusters induces a clear decrease of CO adsorption, which matches with the previous reports on ultra-small clusters (*n*≤6) [39,40]. Moreover, the Au$_x$Ag$_y^+$ nanoclusters in the even-atom disappeared when the 1% CO gas was introduced into the system (Figure 4a and b). These Au$_x$Ag$_y^+$ nanoclu-

sters in the even-atom may transform to the odd-atom ones *via* the dissociation of one Au and Ag atom during reacting with CO, indicating that the CO adsorption energies are larger than the activation energies for a metal atom removed from the intermediate cluster carbonyl complexes for these even-numbered alloy clusters [40]. In addition, *in-situ* adsorption of acetylene (C$_2$H$_2$) gas with Au nanoclusters was further performed and similar distinct size- and charge-hierarchy activity of clusters was observed (Figure S10). Therefore, global stability and activity profiling of metal nanoclusters is successfully achieved by incubating with gas reagents coupled with *in-situ* HRMS monitoring. Hence, the size factor (single atom to clusters of hundreds of atoms), constitution (*e.g.*, foreign dopants (S and P) and alloy), and the charge state (1+ to 3+) of the nanoclusters can be globally profiled to screen out the highly stable and active nanoclusters with unique geometric and electronic structures.

4   Conclusions

In this study, we demonstrate the ultraviolet laser dissociation of MPC precursors within HRMS as a stable and efficient strategy for *in-situ* generation and global characteri-
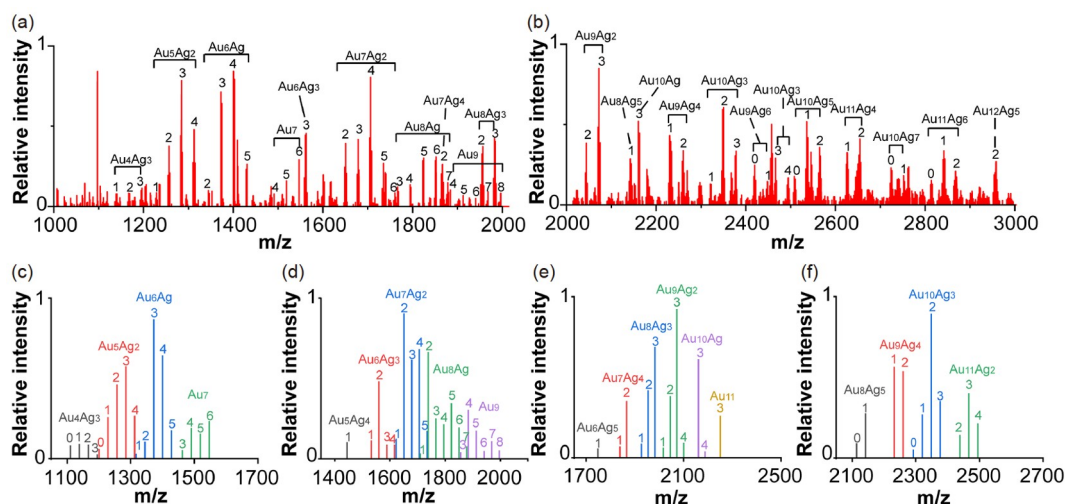
Figure 4 The global activity profiling of AuAg alloy nanoclusters by incubating with CO gas reagent (20 mTorr, 1 $v\%$ CO and 99 $v\%$ N$_2$), followed with *in-situ* HRMS detection. (a, b) The spectra of AuAg nanoclusters interacting with CO; (c–f) the extracted spectra for [Au$_x$Ag$_y$]$^+$ nanoclusters with the metal atom number ($x + y$) of 7 (c), 9 (d), 11 (e) and 13 (f). n indicates the number of CO adsorbed on the alloy nanoclusters. The detection conditions are the same as that in Figure 1 (color online).

zation of bare metal nanoclusters with diverse physical and chemical properties. The sizes, constitutions, and charge states of the metal clusters can be feasibly tuned. The generation of metal nanoclusters provides extremely valuable resources as active cluster candidates to screen out the ones with unique geometric/electronic structure and activity. Thus, combining the merits of ultraviolet laser dissociation and HRMS, we could generate a complex mixture of metal nanoclusters with different sizes, constitutions, and charge states, followed by accurate constitution characterization and global activity profiling.

The merits of this nanocluster study include: (1) the stability of metal clusters with consecutive size (precise metal atoms), diverse constitution (with S and P dopants or alloy) and multiple charge states (*e.g.*, 1+, 2+, 3+) can be systematically investigated; (2) the metal nanoclusters can be mediated by the selection of the dissociation precursors (gold and alloy MPC), which could be applicable to other MPC precursors [41,42]; (3) the global activity profiling of metal clusters could be easily achieved *via* incubating with gas reagents (CO and C$_2$H$_2$) coupled with HRMS characterizations to screen out the ones with unique geometric/electronic structure and activity, such as the crucial transition points of two consecutive clusters with distinct activity. Compared with previous studies of metal clusters, this method greatly improves the throughput for diverse metal nanocluster production and global property profiling, especially the novel multiply charged (+2 and +3) and hetero-atoms (S and P)-doped clusters can be conveniently produced and characterized. Professional data processing software may be developed in the near future for the complex metal-cluster spectra analysis, which will further improve the throughput of cluster property profiling. Overall, this new paradigm of

nanocluster study may greatly promote the discovery and application of active metal nanoclusters for wide applications such as the energy conversion catalysis.

Conflict of interest   The authors declare no conflict of interest.

Supporting information   The supporting information is available online at http://chem.scichina.com and http://link.springer.com/journal/11426. The supporting materials are published as submitted, without typesetting or editing. The responsibility for scientific accuracy and content remains entirely with the authors.

1   Chakraborty I, Pradeep T. *Chem Rev*, 2017, 117: 8208–8271
2   Parent DC, Anderson SL. *Chem Rev*, 1992, 92: 1541–1565
3   Wilcoxon JP, Abrams BL. *Chem Soc Rev*, 2006, 35: 1162–1194
4   Parker JF, Fields-Zinna CA, Murray RW. *Acc Chem Res*, 2010, 43: 1289–1296
5   Li G, Jin R. *Acc Chem Res*, 2013, 46: 1749–1758
6   Jia Y, Luo Z. *Coord Chem Rev*, 2019, 400: 213053
7   Kang X, Zhu M. *Chem Soc Rev*, 2019, 48: 2422–2457
8   Luo Z, Castleman Jr. AW, Khanna SN. *Chem Rev*, 2016, 116: 14456–14492
9   Yao Q, Feng Y, Fung V, Yu Y, Jiang DE, Yang J, Xie J. *Nat Commun*, 2017, 8: 1555
10 Irion MP, Selinger A, Schnabel P. *Z Phys D Atoms Molecules Clusters*, 1991, 19: 393–396
11 Dietz TG, Duncan MA, Powers DE, Smalley RE. *J Chem Phys*, 1981, 74: 6511–6512
12 Bondybey VE, English JH. *J Chem Phys*, 1981, 74: 6978–6979
13 Duncan MA. *Rev Sci Instruments*, 2012, 83: 041101
14 Haberland H, Mall M, Moseler M, Qiang Y, Reiners T, Thurner Y. *J Vacuum Sci Tech A-Vacuum Surfs Films*, 1994, 12: 2925–2930
15 Grammatikopoulos P, Steinhauer S, Vernieres J, Singh V, Sowwan M.

Adv Phys-X, 2016, 1: 81–100

16 Vezmar I, Alvarez MM, Khoury JT, Salisbury BE, Shafigullin MN, Whetten RL. *Z für Physik D Atoms Molecules Clusters*, 1997, 40: 147–151

17 Arnold RJ, Reilly JP. *J Am Chem Soc*, 1998, 120: 1528–1532

18 Black DM, Crittenden CM, Brodbelt JS, Whetten RL. *J Phys Chem Lett*, 2017, 8: 1283–1289

19 Higaki T, Li Q, Zhou M, Zhao S, Li Y, Li S, Jin R. *Acc Chem Res*, 2018, 51: 2764–2773

20 Qian H, Jin R. *Chem Mater*, 2011, 23: 2209–2217

21 Lin J, Li W, Liu C, Huang P, Zhu M, Ge Q, Li G. *Nanoscale*, 2015, 7: 13663–13670

22 Zheng K, Zhang J, Zhao D, Yang Y, Li Z, Li G. *Nano Res*, 2019, 12: 501–507

23 Loos M, Gerber C, Corona F, Hollender J, Singer H. *Anal Chem*, 2015, 87: 5738–5744

24 Liu C, Abroshan H, Yan C, Li G, Haruta M. *ACS Catal*, 2015, 6: 92–99

25 Chen Y, Liu C, Abroshan H, Li Z, Wang J, Li G, Haruta M. *J Catal*, 2016, 340: 287–294

26 Katakuse I, Ichihara T, Fujita Y, Matsuo T, Sakurai T, Matsuda H. *Int J Mass Spectrometry Ion Processes*, 1985, 67: 229–236

27 Luo Z, Reber AC, Jia M, Blades WH, Khanna SN, Castleman AW. *Chem Sci*, 2016, 7: 3067–3074

28 Chen S, Xiong L, Wang S, Ma Z, Jin S, Sheng H, Pei Y, Zhu M. *J Am Chem Soc*, 2016, 138: 10754–10757

29 de Heer WA. *Rev Mod Phys*, 1993, 65: 611–676

30 Ferrando R, Jellinek J, Johnston RL. *Chem Rev*, 2008, 108: 845–910

31 Taketoshi A, Haruta M. *Chem Lett*, 2014, 43: 380–387

32 Stratakis M, Garcia H. *Chem Rev*, 2012, 112: 4469–4506

33 Wallace WT, Whetten RL. *J Phys Chem B*, 2000, 104: 10964–10968

34 Neumaier M, Weigend F, Hampe O, Kappes MM. *J Chem Phys*, 2005, 122: 104702

35 Häkkinen H. *Chem Soc Rev*, 2008, 37: 1847–1859

36 Häberlen OD, Chung SC, Stener M, Rösch N. *J Chem Phys*, 1997, 106: 5189–5201

37 Wu X, Senapati L, Nayak SK, Selloni A, Hajaligol M. *J Chem Phys*, 2002, 117: 4010–4015

38 Bürgel C, Reilly NM, Johnson GE, Mitrić R, Kimble ML, Castleman Jr. AW, Bonačić-Koutecký V. *J Am Chem Soc*, 2008, 130: 1694–1698

39 Neumaier M, Weigend F, Hampe O, Kappes MM. *Faraday Discuss*, 2008, 138: 393–406

40 Neumaier M, Weigend F, Hampe O, Kappes MM. *J Chem Phys*, 2006, 125: 104308

41 Zheng XY, Kong XJ, Zheng Z, Long LS, Zheng LS. *Acc Chem Res*, 2018, 51: 517–525

42 Yuan P, Chen R, Zhang X, Chen F, Yan J, Sun C, Ou D, Peng J, Lin S, Tang Z, Teo BK, Zheng LS, Zheng N. *Angew Chem Int Ed*, 2019, 58: 835–839